

The Massive Expansion and Spatial Transformation of Potentially Contaminated Land Across China in 1990–2020 Observed from Remote Sensing and Big-data

DOU Yinyin¹, GUO Changqing¹, KUANG Wenhui¹, CHI Wenfeng², LEI Mei¹

(1. *Institute of Geographic Sciences and Natural Resources Research, Chinese Academy of Sciences, Beijing 100101, China*; 2. *School of Resources and Environmental Economics, Inner Mongolia University of Finance and Economics, Hohhot 010017, China*)

Abstract: Identifying and monitoring the spatiotemporal patterns of potentially contaminated land (PCL) in China is a key concern of ecological governance. However, the dynamics of PCL's expansion remain unclear nationwide. Integrating high-resolution remote sensing images, a land-use/cover change database, crawler data from websites, and other multisource data, we produced a new dataset of China's PCL in 1990, 2000, 2010, and 2020 using data fusion technology. Then we analyzed the spatiotemporal patterns of China's PCL from 1990 to 2020. Our study shows that the acquired vector dataset of China's PCL is of high quality and reliability, with an overall accuracy of 93.21%. The area of China's PCL has kept growing for the past 30 years, and the growth rate was especially rapid during 2000–2010, 2.32 and 6.13 times as rapid as that during 1990–2000 and 2010–2020, respectively. PCL has also been trending toward higher aggregation over markedly enlarged areas and has transferred progressively from north and southeast of China to northwest and southwest of China and Qinghai-Tibet Plateau. The patterns of China's PCL have been driven by the joint factors of policies, mineral resources, economy, and others, among which policies and the economy have contributed more prominently to the long-term transition. Our study promotes the access to high-quality spatial data of PCL to facilitate environmental governance of mine wastes, pollution and land management.

Keywords: potentially contaminated land (PCL); remote sensing mapping; mining area; ecological risk; environmental governance

Citation: DOU Yinyin, GUO Changqing, KUANG Wenhui, CHI Wenfeng, LEI Mei, 2022. The Massive Expansion and Spatial Transformation of Potentially Contaminated Land Across China in 1990–2020 Observed from Remote Sensing and Big-data. *Chinese Geographical Science*, 32(5): 776–791. https://doi.org/10.1007/s11769-022-1300-6

1 Introduction

A series of social and environmental issues arising from industrial activities has received growing attentions (Sonter et al., 2017; Werner et al., 2020; Luckeneder et al., 2021). Recognizing and understanding the spatiotemporal characteristics and hotspots of industrial and mining areas are key parts of ecological environment

construction (Palmer et al., 2010; Sonter et al., 2020), and are essential in attaining the sustainable development goals (SDGs) by 2030 (UN, 2015; Endl et al., 2021). Roughly 1% of global land is affected by industrial and mining activities (Walker, 1999). For example, remote sensing monitoring has found the area of global mine lots to be 57 277 km² (Maus et al., 2020). Industrial and mining activities could leave a hugely negative

Received date: 2022-05-14; accepted date: 2022-07-15

Foundation item: Under the auspices of the National Key Research and Development Program (No. 2018YFC1800103, 2018YFC1800106)

Corresponding author: KUANG Wenhui. E-mail: kuangwh@igsnr.ac.cn

© Science Press, Northeast Institute of Geography and Agroecology, CAS and Springer-Verlag GmbH Germany, part of Springer Nature 2022

impact on the environment by not only severely deteriorating or devastating the natural ecosystem (Sonter et al., 2017; Luckeneder et al., 2021), but also adversely affecting human health with water and air pollutants (Palmer et al., 2010; Rojano et al., 2018). Therefore, it is imperative to recognize and clarify the spatiotemporal patterns of potentially contaminated land (PCL) and identify their hotspots, which will provide an important basis for ecological governance and control.

With the increasing development of industrialization in China, the number and scale of PCL are growing rapidly, bringing about a series of environmental pollutions and public health risks (Yang et al., 2014; Li et al., 2021; Song et al., 2021). In particular, serious problems include the heavy metal pollution of soil around industrial and mining processes (Wang et al., 2011). According to a general survey of soil pollution in China, 20%–37% of the soil positioned around PCL across all of China suffered from excessive pollution, and approximately 2×10^7 ha farmland soils were contaminated, resulting in an economic loss of up to 2 billion yuan (RMB) during 2005–2013 (MEE, 2014). Therefore, timely recognition of the spatial patterns and hotspots and rapid relocation of China's PCL are essential to attaining the SDGs.

Numerous methods have been applied recently in information acquisition from and mapping of PCL (Rampanelli et al., 2021; Sonter et al., 2020; Tang et al., 2021). For example, the traditional field investigation (Nortcliff, 2001), the combination of remote sensing image interpretation and actual measurement investigation (Kimijima et al., 2021), the object-oriented method (Zeng et al., 2017), and deep learning (Gallwey et al., 2020) have provided vital techniques and technologies for timely and accurately acquiring information about PCL. However, due to current technological limitations, most acquisition methods are targeted at acquiring information from a single type of area (Peng et al., 2019; Maus et al., 2020), such as coal mining areas (Pericak et al., 2018) and metal mining areas (Owusu-Nimo et al., 2018). With the burgeoning development in GIS techniques, location-based service technology, and web crawler technology, the development in satellite remote sensing and big-data technologies has provided novel techniques and methods for solving this problem (Boldi et al., 2004; Pericak et al., 2018). These approaches have overcome the disadvantages of heavy workload

and time consumption in traditional position sampling while demonstrating the advantages of speed, economy, and fineness in PCL recognition (Pericak et al., 2018). Numerous scholars have used web crawler technology for data crawling and visualized analysis (Li et al., 2010; Kausar et al., 2013; Kim et al., 2019). Therefore, the combination of remote sensing technology with web crawler and/or other technologies can not only acquire more detailed information about the types of areas but also provide favorable technical support for quickly recognizing PCL.

Some scholars have researched the spatiotemporal characteristics of industrial and mining areas at the global, regional, national, and more diverse scales (Bernhardt et al., 2012; Sonter et al., 2017; Werner et al., 2020; Ahmed et al., 2021; Cribari et al., 2021; Saley et al., 2021; Tang et al., 2021). For example, they have performed analyses and mapping of the distributions of mining areas at global scale (Werner et al., 2020), analyzed the mining land extension in sub Saharan Africa at regional scale (Ahmed et al., 2021), and analyzed the evolution characteristics of the gold mine areas in Niger (Saley et al., 2021). However, recognition of spatiotemporal patterns and hotspots of different types of PCL at different scales in China remains unclear, given that the existing studies are mostly targeted at the evolution of areas at a single scale and of a single type (Li et al., 2020; Tang et al., 2021). For example, some have analyzed the pattern of potentially contaminated sites in China at the national scale (Jiang et al., 2021), some have analyzed spatiotemporal variations in coal mining and restoration and their ecological environment effects in the Qinghai-Tibet Plateau (QTP) at regional scale (Yuan et al., 2021), and some have analyzed the spatiotemporal evolution of the mine lots in six counties of Gansu Province, China (Li et al., 2020). Therefore, it is urgent to grasp the spatiotemporal evolution characteristics and hotspots of different types of PCL across China at multiple scales.

Our study aimed to analyze the spatiotemporal patterns and hotspots of China's PCL during 1990–2020 based on acquisition of the information about China's PCL. First, we acquired the dataset of China's PCL in 1990, 2000, 2010, and 2020 based on multisource data fusion technology by using high-resolution remote-sensing images, a land-use/cover change database, crawler data from websites, Open Street Map (OSM) data, and

field investigation data. Second, we analyzed the spatiotemporal patterns and hotspots of China's PCL during 1990–2020. Third, we examined the influencing factors of PCL relocation and their influences on the ecological environment. This study provides scientific information for ecological governance.

2 Materials and Methods

2.1 Study area and data sources

Considering the characteristics and disparities across China's geographic regions, we divided the whole territory

of China into six zones for better depiction of the spatiotemporal evolution and migration patterns of China's PCL. The six geographical zones include Northeast China (NE), North China (N), Southeast China (SE), Southwest China (SW), Northwest China (NW), and Qinghai-Tibet Plateau (QTP) (Kuang et al., 2022). Taiwan Province of China was excluded due to data acquisition limitations (Fig. 1).

The data sources contain six major types, including a land-use/cover change database, OSM data, data from web crawler, high-resolution remote-sensing images, field investigation data, and other auxiliary data (Fig. 1).

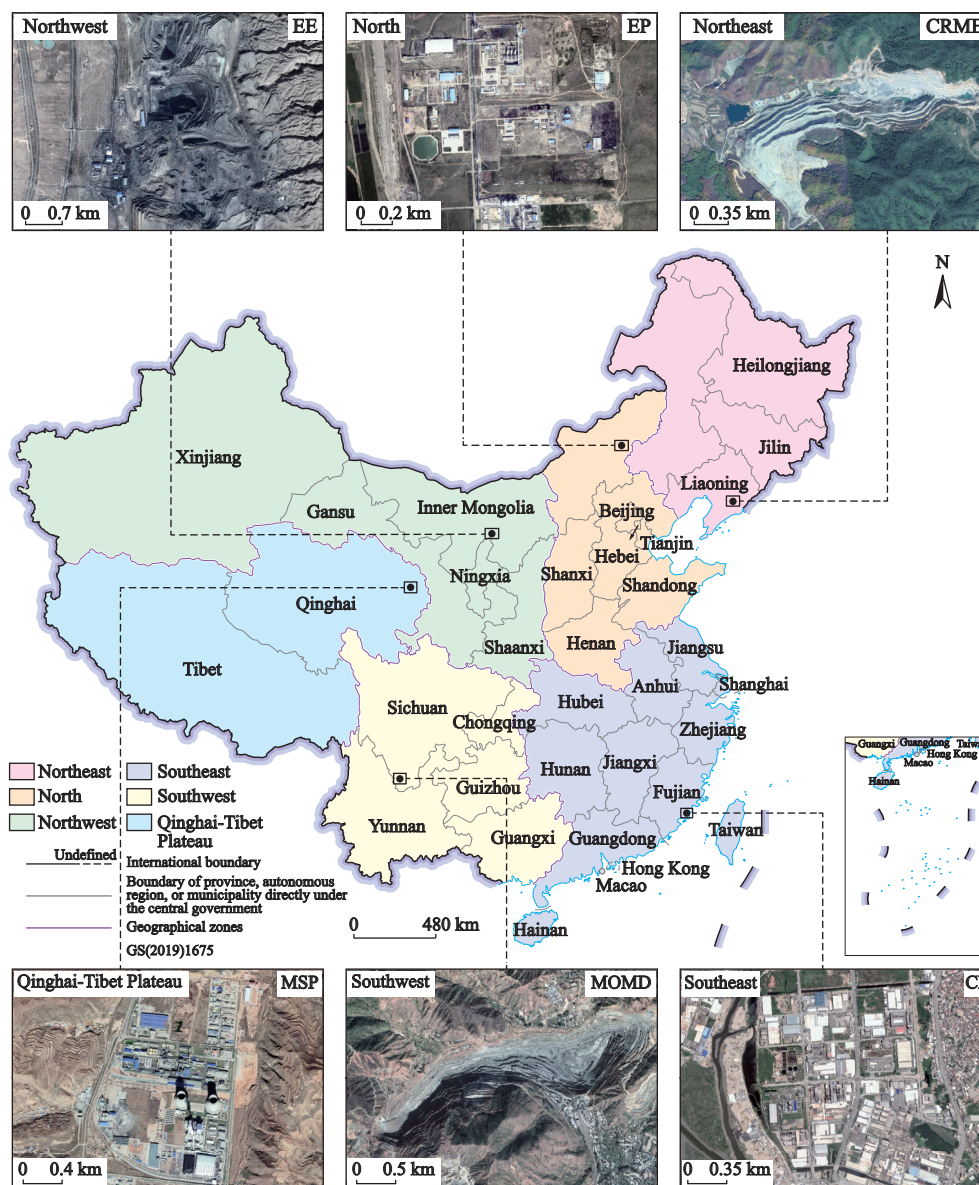


Fig. 1 Study areas and six types of potentially contaminated land in China. EE, energy exploitation; EP, energy processing; CRME, chemical raw material exploitation; MSP, metal smelting & processing; MOMD, metal ore mining & dressing; CP, chemical processing

Among them, China's Land Use/cover Dataset (CLUD) was downloaded from the Institute of Geographic Sciences and Natural Resources Research, Chinese Academy of Sciences (<http://www.igsnr.ac.cn/>). This dataset contains the CLUD vector data from 1990, 2000, 2010, and 2020, and includes six Level-I types and more than 25 Level-II types, with data accuracy higher than 92% (Kuang et al., 2016; Ning et al., 2018). The OSM data of 2020 was obtained from the freely accessible website of OSM (<https://www.openstreetmap.org>). The high-resolution remote-sensing images mainly include GaoFen-2 images (GF-2) of 2016 and Google Earth images of 1990, 2000, 2010, and 2020. GF-2 images were obtained from the Institute of Remote Sensing and Digital Earth, Chinese Academy of Sciences (<http://www.ceode.cas.cn/>), with a spatial resolution of 1 m, whereas the Google Earth image data were downloaded from the website of Google Earth (<http://google-earth.en.softonic.com/>), with spatial resolutions of 0.5 m, 1.0 m, and 2.0 m. The data from a web crawler were predominantly in the directories of national industrial enterprises for 1990–2020, namely the public information crawled from the website of national pollutant emission permit management information (<http://permit.mee.gov.cn/>) based on web crawler technology (Chakrabarti et al., 1999). The crawled data form the spotty spatial distribution information about national industries and enterprises based on data cleansing and screening. The field investigation data contain geospatial position, type, and scale of areas from about 2200 sampling points acquired by the Institute of Geographic Sciences and Natural Resources Research, Chinese Academy of Sciences (Zhang et al., 2021). The auxiliary data contain the national administrative division data at a scale of 1 : 1 000 000, from the National Geomatics Center of China (<http://www.ngcc.cn/>).

2.2 Classification of potentially contaminated land (PCL)

The industrial ore mining areas in this research included open-pit mines, ore dressing infrastructures, waste ore heaps, and ore tailing storage facilities, which can be delimited in the publicly accessible Google Earth images through visual interpretation (Werner et al., 2020). The industrial ore processing areas are the sites with resource exploitation and processing as the leading industry, including industrial parks and their ancillary

facilities. First, the initial boundaries of mining and processing land are fused with the point distribution about industries and enterprises based on high-resolution remote sensing images, namely the Google Earth images (supplemented by GF-2 and Landsat images). The spatial relationship between the initial PCL boundary (mining land and processing land) and the point distributions of industrial enterprises was obtained using overlay spatial analysis method. Second, the industry type with the largest number of industrial enterprises in the patch is classified as the types of PCL. Finally, the PCL are divided into two Level-I types and six Level-II types, referring to relevant studies (Kuang et al., 2016; Ning et al., 2018; Li et al., 2021; Rampanelli et al., 2021) and existing taxonomical systems 'Land-Use Status Classification (GB/T 21010–2017)' and 'National Industries Classification (GB/T 4754–2017)'. Level-I types include two types—mining and processing—whereas Level-II types include six types: metal ore mining and dressing, metal smelting and processing, energy exploitation, energy processing, chemical raw material exploitation, and chemical processing (Table 1, Fig. 1).

2.3 Acquisition of the datasets about China's PCL

To implement scientific spatial measurement of PCL, remote sensing recognition of PCL was carried out by dividing the taxonomical system to acquire the vector datasets about China's PCL during 1990–2020. In accordance with our previous research (Guo et al., 2022), the acquisition of these data includes two links (mining land and processing land) and three steps (Fig. 2). First, the initial boundaries of mining land were obtained from the rural industrial land (Zhang et al., 2021) extracted by CLUD. The initial boundary information about processing land was sourced from the land use extracted by OSM based on keyword retrievals (industry, park, development zone, etc.) (Guo et al., 2022). The network data were crawled using web crawler technology, and the spotty distribution information about industries and enterprises (mainly including enterprise name, license or registration number, address of production and operation site, geographical location, industry category, establishment date, business term, and main pollutant category) was acquired after data cleansing, screening, and spatialization. Next, the multisource data fusion based on high-resolution remote-sensing images, namely Google Earth images (supplemented by GF-2 and Land-

Table 1 Classification of potentially contaminated land (PCL)

Level-I type	Level-II type	Main content
Mining	Metal ore mining & dressing	Areas for minerals predominated by ferrous metals, nonferrous metals and other metal mineral resources, including the mining area, tailings reservoir, stacking yard, dumping site, and their ancillary facilities
	Energy exploitation	Areas for minerals predominated by coal, coalbed methane, bone coal, oil shale, petroleum, natural gas, and other fossil fuel resources, including the mining area, tailings reservoir, stacking yard, dumping site, and their ancillary facilities
	Chemical raw material exploitation	Areas for minerals predominated by chemical, fertilizer minerals, and other nonmetal chemical raw material mineral resources, including the mining area, tailings reservoir, stacking yard, dumping site, and their ancillary facilities
Processing	Metal smelting & processing	Contiguous regions where the areas dominated by the smelting and processing industry of ferrous, nonferrous, and other metals are centralized
	Energy processing	Contiguous regions where the areas dominated by the processing industry of coal, crude oil, and other fossil fuels are centralized
	Chemical processing	Contiguous regions where the areas dominated by the manufacturing industry of inorganic chemicals, organic chemicals, fertilizers, pesticides, and other chemical raw materials and products are centralized

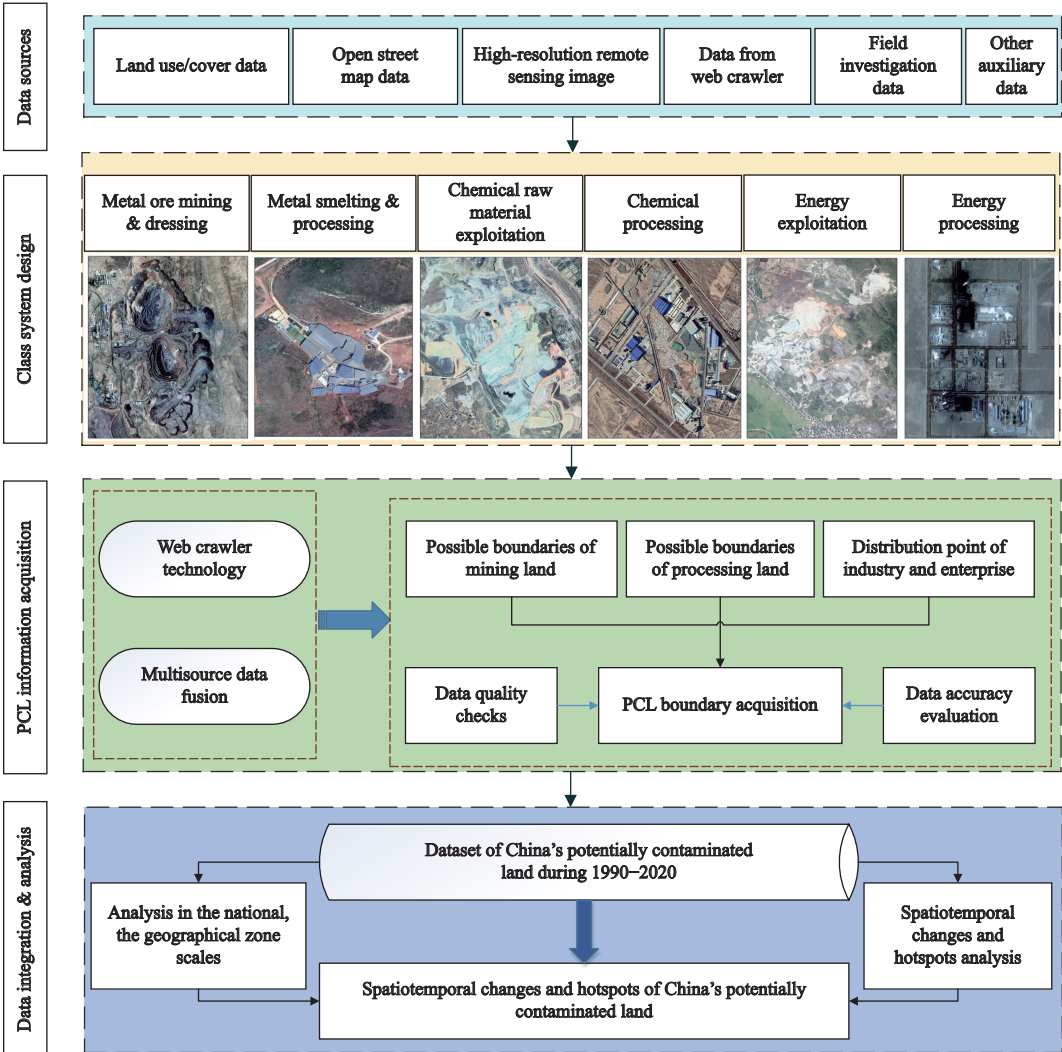


Fig. 2 Flow chart of the study

sat images) and the spotty distribution information about industries and enterprises, traversed the initial PCL boundaries (mining land and processing land) and delimited the land patch type and integrated attribute in-

formation based on the industry type with the largest number of industrial enterprises in the patch. In this process, the PCL boundary was revised through visual interpretations to obtain high-precision site boundary information (Guo et al., 2022). Finally, based on previous research (Zhang et al., 2014, 2021; Guo et al., 2022), the accuracy of the data about China's PCL was verified by using high-resolution images combined with the field investigation data.

2.4 Analysis of the changes of China's PCL

To better describe the evolution and migration patterns at different scales of PCL, the areas were classified into three types: small-scale areas ($< 1 \text{ km}^2$), medium-scale areas ($1\text{--}10 \text{ km}^2$), and large-scale areas ($>10 \text{ km}^2$). The changes in PCL were analyzed in terms of such indicators as the speed of change, proportion of change, and intensity of change.

2.4.1 Speed of change of PCL

The speed of change of PCL (IMS) refers to the annual average variation in size of PCL within a specific time interval, as given by the formula below:

$$IMS_{t_1-t_2} = \frac{IMS_{t_2} - IMS_{t_1}}{t_2 - t_1} \quad (1)$$

where $IMS_{t_1-t_2}$ is the speed of area change (km^2/yr) of PCL within the interval from t_1 to t_2 ; IMS_{t_2} and IMS_{t_1} are the areas (km^2) of PCL at points-in-time t_2 and t_1 , respectively.

2.4.2 Proportion of change of PCL

The proportion of change of PCL (IMP) refers to the proportion of the variation in area of PCL within the specific time interval over the area of PCL at the start year, as given by the formula below:

$$IMP_{t_1-t_2} = \frac{IMS_{t_2} - IMS_{t_1}}{IMS_{t_1}} \times 100\% \quad (2)$$

where $IMP_{t_1-t_2}$ is the proportion of change (%) of PCL within the interval from t_1 to t_2 .

2.4.3 Intensity of change of PCL

The intensity of change of PCL (IMI) refers to the proportion of variation in area of PCL over the $10 \text{ km} \times 10 \text{ km}$ grid cells (100 km^2) within the specific time interval, as given by the formula below (Guo et al., 2022):

$$IMI_{t_1-t_2} = \frac{IMS_{t_2} - IMS_{t_1}}{100} \times 100\% \quad (3)$$

where $IMI_{t_1-t_2}$ is the intensity of change (%) of PCL

within the interval from t_1 to t_2 .

2.5 Recognition of hotspots of China's PCL

The distribution aggregation effect was further detected in the county-level dimension to identify the distribution hotspots of China's PCL. The distribution heat index data of PCL were acquired for analysis on the hotspot distribution characteristics of China's PCL using the Adaptive Spatial Clustering Algorithm based on Delaunay Triangulation (ASCDT) method (Deng et al., 2011).

The kernel density estimation of PCL was performed with optimized ASCDT. Compared with traditional kernel density estimation algorithms (Okabe et al., 2009), ASCDT lays more emphasis on the spatial interrelation and morphological distribution of areas (Deng et al., 2011). Based on optimized ASCDT, we obtained the values of spatial distribution density of point features of PCL across China, and calculated the heat index of PCL. The formula is as follows:

$$R_i = \frac{D_i - D_{\min}}{D_{\max} - D_{\min}} \quad (4)$$

where R_i is the value of the spatial distribution heat index of PCL corresponding to the i th grid cell, ranging within 0–1; D_i is the value of distribution density of PCL corresponding to the i th grid cell; D_{\min} and D_{\max} refer to the minimum and maximum of all values of D_i , respectively.

The verification data of hotspots of China's PCL was obtained from the field survey data and the data on the concentration area of PCL publicly released by the Ministry of Ecology and Environment of the People's Republic of China. We compared the verification points with the identification of hotspots and used the ratio of the number of the verification points in hotspot areas to the total number of verification points as the verification result of the hotspots of China's PCL.

The overall accuracy of the data about PCL was verified by using random sampling combined with the ground survey method, applying high-resolution images and field investigation data. The accuracy assessment of China's PCL in 1990, 2000, 2010 and 2020 were selected (the number of samples was about 10% of the total data) 2220, 2731, 3710, and 3121 sampling points for accuracy verification, respectively, and the accuracy assessment was carried out using the correct rate and

transfer matrix. The correct rate is the ratio of correctly identified type samples to the total number of samples.

3 Results

3.1 Accuracy of China's PCL dataset

The accuracy of the PCL dataset was reassessed in six geographical zones of China based on previous research (Guo et al., 2022). With random selection and field survey data, we generated 2220, 2731, 3710, and 3121 sampling points from among the data products about China's PCL in 1990, 2000, 2010, and 2020, respectively, and carried out data accuracy evaluation (Fig. 3). The accuracies of the products were 92.61%, 92.60%, 92.99%, and 94.62%, respectively, and the overall accuracy of the data products about China's PCL reached 93.21% (Table 2).

In the geographical zones, the overall accuracies were 93.87%, 95.08%, 92.11%, 91.06%, 94.43%, and 93.54% for N, NE, NW, SE, SW, and QTP, respectively. Among them, the SE and NW zones had relatively low accuracies, both falling below the national average (Table 2). Two main types of problems may exist with our multimethod. First, in the arid and semi-arid climate zones, it is difficult to distinguish the subsurface of potentially polluted sites from desert and bare soil, which easily leads to the phenomenon of mapping errors and omissions, resulting in a low average accuracy of the NW zone. Second, it is difficult to accurately

map the energy processing sites interspersed with urban land and rural settlements in the high-speed economic development areas, yielding a relatively low overall accuracy of the SE zone.

3.2 Evolution characteristics of China's PCL

3.2.1 Spatial pattern of China's PCL in 2020

The area of China's PCL is 13 856.08 km², over which the chemical processing areas account for approximately one-third (Table 3). In 2020, China's PCL accounted for 0.14% of the country's total territorial area. Within these areas, chemical processing took up the largest area of 4852.11 km², accounting for 35.02% and was distributed mostly in the SE and N zones (Fig. 4).

China's PCL areas are significantly different in size, with small-scale areas predominately in mining and large-scale areas predominately affected by processing (Fig. 4, Table 3). In 2020, the total of small-scale areas was 1958.82 km², accounting for 14.14% of the total area of PCL; moreover, metal ore mining and dressing areas and energy exploitation areas preponderated, with areas of 1089.88 km² and 649.31 km², respectively. While the metal ore mining and dressing areas were distributed mostly in the SE, N, and NW zones, the energy exploitation areas were centralized in the NW and N zones (Fig. 4). The total of large-scale areas was 8330.40 km², accounting for 60.12% of the total area of PCL, predominated by chemical processing (3550.49 km²) and metal smelting and processing (3043.14 km²),

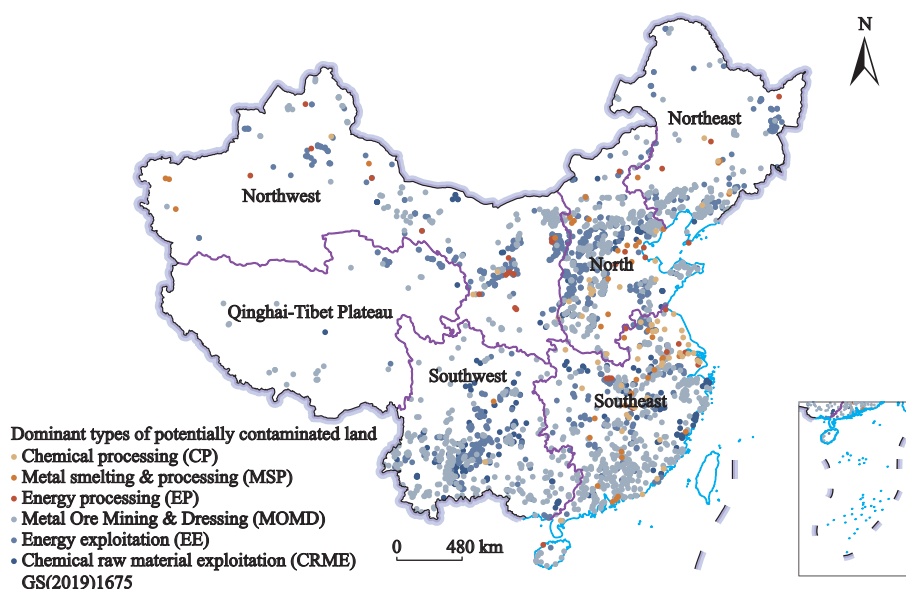


Fig. 3 Spatial distribution of sampling points in China. Not including Taiwan Province of China due to data acquisition limitations

Table 2 Accuracy of potentially contaminated land (PCL) in different geographical zones in different years

Zone in China	Index	1990	2000	2010	2020	Overall accuracy ^a
North	Total number of samples	643	831	1030	918	93.87
	Correct number of samples	594	774	967	882	
	Incorrect number of samples	49	57	63	36	
	Producer's accuracy / %	92.38	93.14	93.88	96.08	
Northeast	Total number of samples	294	380	400	334	95.08
	Correct number of samples	277	357	383	322	
	Incorrect number of samples	17	23	17	12	
	Producer's accuracy / %	94.22	93.95	95.75	96.41	
Northwest	Total number of samples	266	336	436	428	92.11
	Correct number of samples	246	308	397	399	
	Incorrect number of samples	20	28	39	29	
	Producer's accuracy / %	92.48	91.67	91.06	93.22	
Southeast	Total number of samples	541	603	973	789	91.06
	Correct number of samples	485	549	887	729	
	Incorrect number of samples	56	54	86	60	
	Producer's accuracy / %	89.65	91.04	91.16	92.40	
Southwest	Total number of samples	432	530	807	599	94.43
	Correct number of samples	413	493	758	570	
	Incorrect number of samples	19	37	49	29	
	Producer's accuracy / %	95.60	93.02	93.93	95.16	
Qinghai-Tibet Plateau	Total number of samples	44	51	64	53	93.54
	Correct number of samples	41	48	58	51	
	Incorrect number of samples	3	3	6	2	
	Producer's accuracy / %	93.18	94.12	90.63	96.23	
Nationwide	Total number of samples	2220	2731	3710	3121	93.21
	Correct number of samples	2056	2529	3450	2953	
	Incorrect number of samples	83	114	96	62	
	Producer's accuracy / %	92.61	92.60	92.99	94.62	

Note: ^a Overall accuracy is the average of data accuracies of 1990, 2000, 2010, and 2020

and centralized in the SE and N zones (Fig. 4, Table 3).

3.2.2 Changes in China's PCL during 1990–2020

China's PCL has been in overall growth for the last three decades, especially during 2000–2010, although with significant differences between the ten-year intervals (Fig. 5, Table 3). The area of PCL has increased by 8715.38 km² at a rate of 290.51 km²/yr, and the increased area mainly stems from the rapid development of chemical processing and metal smelting and processing. The decade 2000–2010 saw the highest growth rate in PCL area, with 59.76% of the increased area contributed from chemical processing and metal smelting and processing. The area of China's PCL increased from

5140.70 km² to 7496.30 km² during 1990–2000. After 2000, China's accession to the WTO and the implementation of China's Western Development Strategy further boosted the growth rate of PCL. The speed of change was 546.72 km²/yr during 2000–2010, 2.32 times that during 1990–2000. After 2010, China released and implemented a series of policies and suggestions on environmental protection and pollution control, strengthening the governance over industrial ore mining and processing. During 2010–2020, the mining areas across China decreased by an average of 161.30 km²/yr.

During the past 30 yr, China's PCL has transformed progressively from predominately small- and medium-

Table 3 Variations in area of China’s potentially contaminated land (PCL) during 1990–2020

Type	Scale of area	Changes in size of area / km ²				Changes in size of area per year / (km ² /yr)	
		2020	1990–2000	2000–2010	2010–2020	1990–2020	1990–2020
Metal ore mining & dressing	Large	241.84	36.67	34.91	77.28	148.86	4.96
	Medium	548.32	207.40	137.49	−276.60	68.29	2.28
	Small	1089.88	366.11	727.22	−963.05	130.28	4.34
Energy exploitation	Large	433.11	122.45	92.73	87.02	302.20	10.07
	Medium	603.87	90.90	234.50	−57.50	267.90	8.93
	Small	649.31	218.03	356.10	−450.22	123.91	4.13
Chemical raw material exploitation	Large	527.58	1.64	224.47	131.88	357.99	11.93
	Medium	73.43	23.56	7.21	−13.96	16.81	0.56
	Small	152.56	59.34	113.49	−147.80	25.03	0.83
Energy processing	Large	534.24	107.53	226.53	142.69	476.75	15.89
	Medium	66.61	11.51	44.17	4.76	60.44	2.01
	Small	3.22	1.77	1.02	0.43	3.22	0.11
Metal smelting & processing	Large	3043.14	251.74	1225.74	623.55	2101.03	70.03
	Medium	1010.85	223.18	350.63	295.52	869.33	28.98
	Small	26.01	13.96	1.34	8.28	23.58	0.79
Chemical processing	Large	3550.49	318.48	1233.89	1057.47	2609.84	86.99
	Medium	1263.78	277.38	453.41	368.55	1099.34	36.64
	Small	37.84	23.95	2.32	4.31	30.58	1.02
All	Nationwide	13,856.08	2355.60	5467.17	892.61	8715.38	290.51

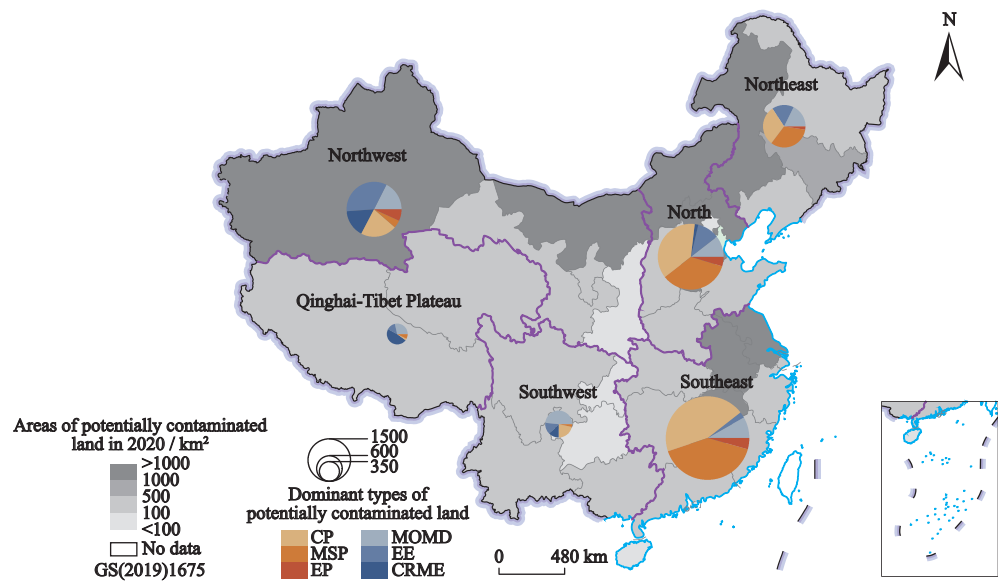


Fig. 4 Spatial patterns of different types of PCL across China in 2020. Not including Taiwan Province of China due to data acquisition limitations. CP, chemical processing; MSP, metal smelting and processing; EP, energy processing; MOMD, metal ore mining and dressing; EE, energy exploitation; CRME, chemical raw material exploitation

scale mining to large-scale processing (Fig. 6, Table 3). The proportion of the area of small- and medium-scale areas over the total area of PCL dropped while the pro-

portion of large-scale areas rose during 1990–2020. Among them, the proportion of the size of small- and medium-scale areas dropped from 54.60% in 1990 to

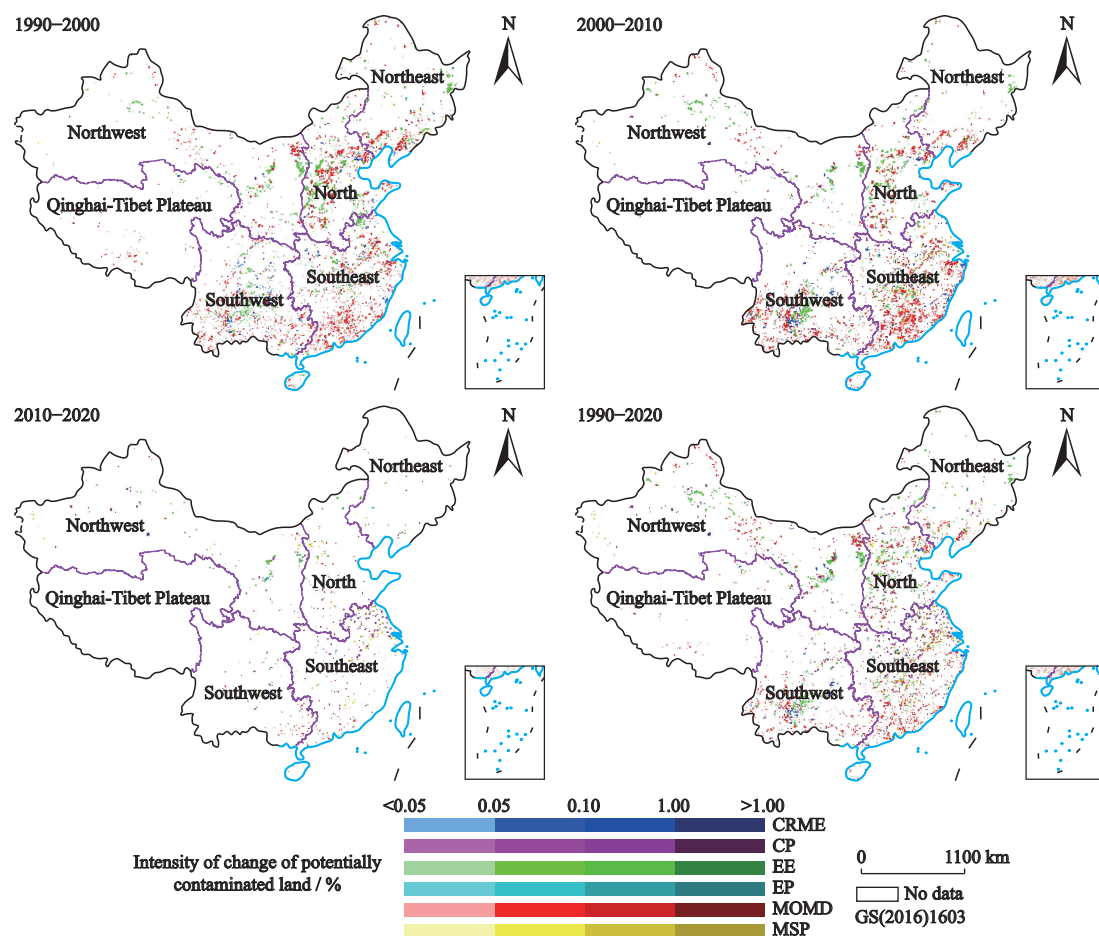


Fig. 5 Intensity of change of China's potentially contaminated land (PCL) in different regions during 1990–2020. Not including Taiwan Province of China due to data acquisition limitations. CRME, chemical raw material exploitation; CP, chemical processing; EE, energy exploitation; EP, energy processing; MOMD, metal ore mining and dressing; MSP, metal smelting and processing

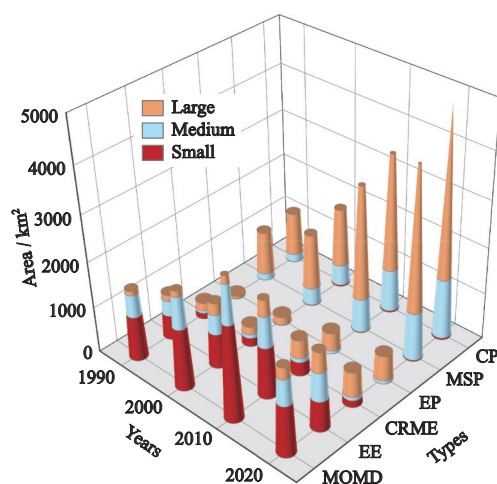


Fig. 6 Evolution of different types of potentially contaminated land (PCL) across China during 1990–2020. CP, chemical processing; MSP, metal ore smelting and processing; EP, energy processing; CRME, chemical raw material exploitation; EE, energy exploitation; MOMD, metal ore mining and dressing

39.88% in 2020, with the greatest contribution from the mining areas, especially from metal ore mining and dressing, whose proportion dropped from 18.67% to 7.78%. On the contrary, the proportion of large-scale areas in the same period rose from 45.40% to 60.12%, with considerable contribution from the processing areas. The proportion of the area of large-scale processing rose from 37.74% to 51.44% during 1990–2020, with the major contribution from the chemical processing and metal smelting and processing areas, whose proportions rose by 6.69 and 4.16 percentage points, respectively (Fig. 6, Table 3).

The spatial pattern of different types of PCL presents distinctive regional variation (Fig. 7). During 1990–2020, medium- and large-scale metal smelting and processing areas transformed progressively from being distributed mostly in the N zone to being distributed mostly in the SE zone (Fig. 7b). The proportion of the area of medium-

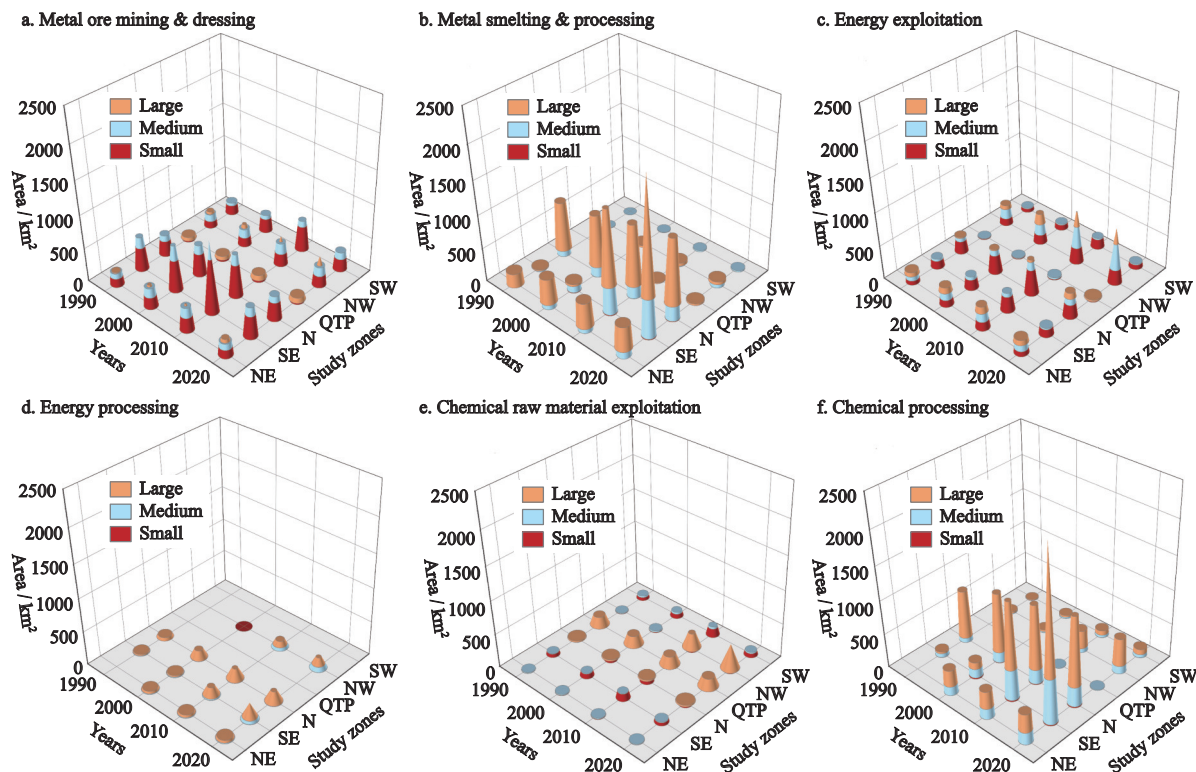


Fig. 7 Area and distribution of China's potentially contaminated land in different zones during 1990–2020. SW, Southwest; NW, Northwest; QTP, Qinghai-Tibet Plateau; N, North; SE, Southeast; NE, Northeast

and large-scale metal smelting and processing areas in the N zone over the total area of metal smelting and processing areas across China dropped from 36.34% in 1990 to 34.48% in 2020; in the same period, the proportion in the SE zone rose from 4.87% to 40.05%, and the size of areas increased from 41.74 km² to 2238.19 km². Medium- and large-scale energy processing areas expanded from the N and SE zones into the NE and NW zones (Fig. 7d). In 1990, these areas constituted proportions of 1.88% and 2.48%, respectively. In 2020, their proportions had increased by 2.80% and 1.56% in the N and SE zones, respectively, and had appeared and risen by 2.37% and 6.82% in the NE and NW zones, respectively. Large-scale chemical raw material exploitation areas were relocated to the NW zone, while medium- and large-scale chemical processing areas based in the N zone were shifted to the SE zone (Fig. 7e). The large-scale chemical raw material exploitation areas in the NW zone took up a proportion of 14.75% by 2020. The proportion of medium- and large-scale chemical processing areas in the N zone rose from 34.19% in 1990 to 37.04% in 2020, while the proportion in the SE zone rose from 9.57% to 43.84%. Metal ore mining and dressing areas have not presented distinctive variation of

pattern since 1990 (Fig. 7a). Small- and medium-scale energy exploitation areas appeared to have been relocated progressively to the NW (Fig. 7c), with their area increasing from 206.27 km² in 1990 to 295.39 km² in 2020.

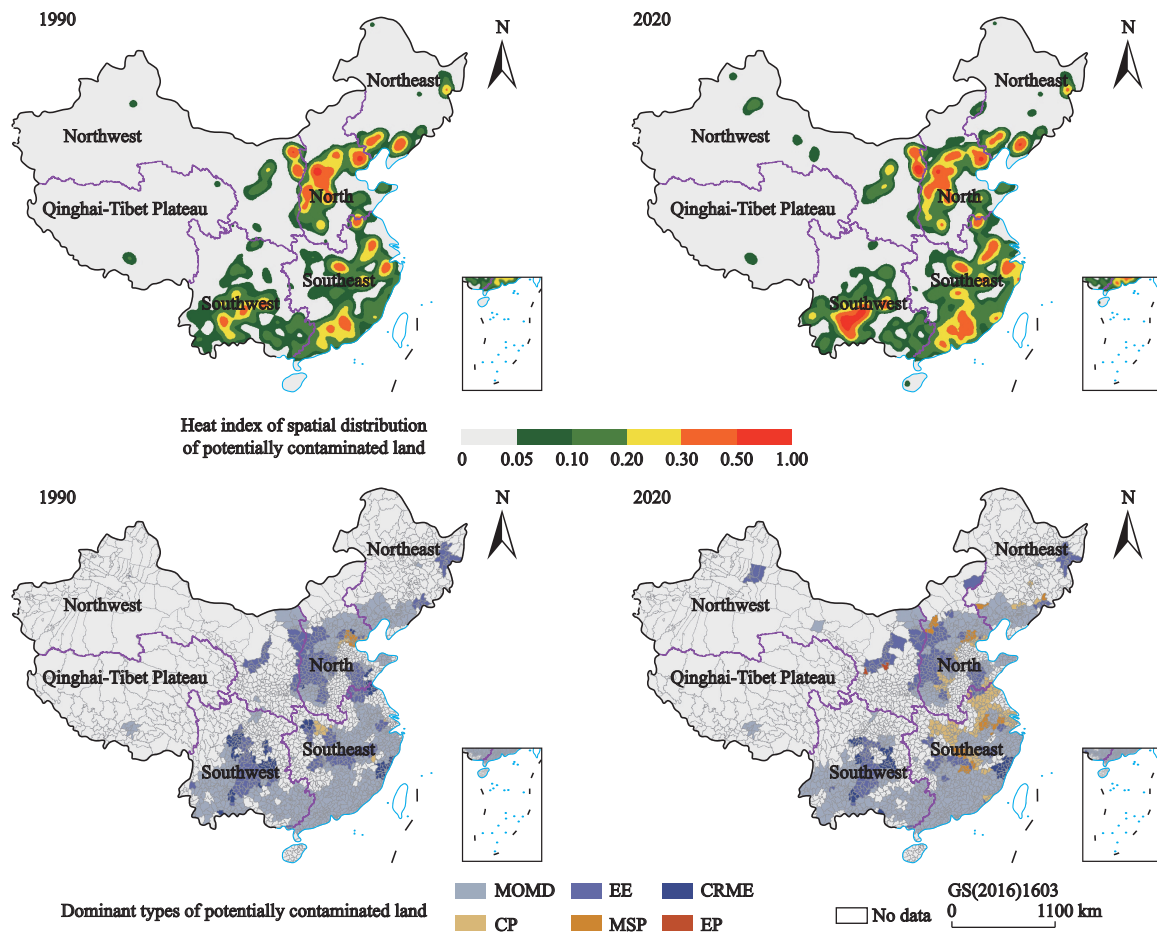
3.3 Hot spots of China's PCL

With field survey data and the data of PCL publicly released by the environmental department, we generated 1691, 2211, 3806, and 2317 verification points from among the data products about the hotspot identification of China's PCL in 1990, 2000, 2010, and 2020, and carried out data accuracy evaluation. The accuracies of hotspots of China's PCL were 86.52%, 86.75%, 87.23%, and 89.17% (Table 4).

China's PCL featured distinctive spatial agglomeration in 2020, with their hotspots agglomerated mostly in the N, SE, and SW zones (Fig. 8). Meanwhile, the spatial distribution of hotspots had considerable differences between different types of PCL. In 2020, 149 county-level administrative regions were dominated by chemical raw material exploitation, accounting for 5.24% and centralized mainly in Sichuan Province, Yunnan Province, Guizhou Province, Fujian Province,

Table 4 Accuracy of the hotspot of China's potentially contaminated land (PCL) in different geographical zones in different years

Zone in China	Total number of samples				Producer's accuracy / %			
	1990	2000	2010	2020	1990	2000	2010	2020
North	469	583	950	610	86.43	86.79	87.30	89.30
Northeast	137	190	297	181	87.10	86.32	86.98	88.79
Northwest	55	82	165	103	87.88	85.37	86.87	89.03
Southeast	649	830	1481	958	86.44	86.87	87.31	88.94
Southwest	373	516	903	455	86.86	87.02	87.38	89.45
Qinghai-Tibet Plateau	8	10	10	10	75.00	80.00	80.00	90.00
Total	1691	2211	3806	2317	86.52	86.75	87.23	89.17

**Fig. 8** Hotspot distributions of potentially contaminated land (PCL) in China during 1990–2020. Not including Taiwan Province of China due to data acquisition limitations. MOMD, metal ore mining and dressing; CP, chemical processing; EE, energy exploitation; MSP, metal smelting and processing; CRME, chemical raw material exploitation; EP, energy processing

and Inner Mongolia Autonomous Region.

China's PCL has rendered an overall intensified tendency of agglomeration over a markedly enlarged sphere since 1990, as well as a phenomenon of transferring progressively to the NW, SW, and QTP zones (Fig. 8). During 1990–2020, China's PCL rendered a further in-

tensified tendency of agglomeration among the city cluster in the middle reach of the Yangtze River, the Guangdong-Hong Kong-Macao Greater Bay Area, and other developed regions. The distribution of PCL showed a tendency of being relocated to Baotou-Ordos-Yulin city cluster and other northwestern regions.

Among all PCL, the large-scale energy processing areas transferred to the QTP zone, centralized in Dagze District, Maizhokunggar County, and Ngagzha County of Tibet Autonomous Region, with their area increasing by 6963.83 km². In the same period, energy exploitation areas had a significant agglomeration effect in the SW zone across 12 counties, such as Nanhua and Yaoan. Meanwhile, the agglomeration sphere of metal smelting and processing areas in the SW zone reached 166 counties, and their area increased by 2993.94 km².

4 Discussion

4.1 Integration with industrial types as an effective way for timely and accurate extraction of PCL

Identifying and obtaining the boundary information about PCL accurately and in a timely manner on a large scale can provide an important data basis for effectively detecting and quantifying the spatiotemporal patterns of PCL. The vector datasets about China's PCL of 1990, 2000, 2010, and 2020 have been developed with remote sensing monitoring over the PCL in satellite images. The geographical databases that were set up include 100 163 vector diagram spots of area boundaries. Compared with the existing data developed and used by research institutes (Jiang et al., 2021), our developed datasets about China's PCL can represent the spatiotemporal patterns of PCL with more details. Our datasets contain not only the information about the positions of areas, such as the longitude and latitude, the names and types of areas, but also the spatial range attributes of area vectors. Meanwhile, the overall accuracy of these PCL databases are above 93% (Table 2), satisfying the requirement for area-related spatiotemporal analysis and regional comparative study. On the other hand, based on the existing vector datasets from CLUD, we have adopted web crawler, data fusion, human-computer interaction interpretation, and other technologies and approaches to acquire the area boundary information, which has shortened data acquisition time and significantly reduced workload and difficulty (Chakrabarti et al., 1999; Kuang et al., 2022). Furthermore, most of the currently released land-use/cover change data products in a large-scale scope (Chen et al., 2015; Liu et al., 2018; Gong et al., 2019, 2020; He et al., 2019; Zhang et al., 2020) have included PCL in such types as urban built-up area, impervious surface, and mining area. Due

to the failure to acquire more detailed information such as related enterprises and environments, the above-mentioned publicly released data products have not recognized different types of PCL.

4.2 Influencing factors for the pattern of PCL

The spatial pattern and migration of China's PCL are joint driving effects of policy, mineral resources, economy, and other factors over the past 30 years, among which policy and economy factors have contributed more prominently to the long time-sequence transition of areas. In the 1990s, small-scale PCL were relatively prominent (average area 0.29 km²) (Fig. 6, Fig. 7), which might be ascribed to plateau landforms, illegal mining, or the mining of small-scale scattered metallic ore deposits (Tang et al., 2020). The quantity and nature of keener oversight have increased the mining costs. Under this circumstance, only the larger-area, high-value ores can be mined economically, driving this industry towards operations producing large-scale PCL (Werner et al., 2020). With the implementation of China's Western Development Strategy, PCL have been relocated to the NW and SW zones, where medium- and large-scale metal ore processing and chemical processing areas have increased by 211.16 km² and 600.34 km², respectively (Fig. 7, Table 3); particularly, the western rural land for industrial ores surged at an alarming rate from 3%–10% in the 1990s to 115% during 2005–2015 (Zhang et al., 2021). After entering the 21st century, China joined the WHO. Under the influence of intensified international competition, the less competitive industries and enterprises were relocated progressively from eastern coastal regions to western regions. During that period, PCL exhibited the spatial characteristic of being relocated to the central and western regions (Fig. 5, Fig. 7). China has taken an active part in global energy governance and successively issued a series of policies and opinions related to ecological governance and supervision to cope with global climate change (SCPRC, 2013, 2015, 2016). Relevant policies have contributed to a significant increase of energy exploitation areas in the NW and QTP zones (Fig. 7). Furthermore, as China's economic growth moves in the green and low-carbon direction, photovoltaic, wind energy, and other renewable energy sources have risen with strong potentials. The power sector is transforming from predominately fossil energy to renewable energy

sources, and the area of large-scale energy exploitation areas in the QTP zone has increased dramatically (Fig. 7, Table 3).

4.3 Hotspots and ecological risks of PCL

Although the distribution of China's industrial ore mining areas obeys the ultimate law of geological enrichment, these areas are centralized in places of population aggregation, lowland regions, and flat regions (Fig. 8) probably due to economic factors. Of the 3.9 million t of wastes generated from nonferrous metal processing in China in 2016, almost 80% came from the northwestern region, Yunnan Province, Inner Mongolia Autonomous Region, Gansu Province, Hunan Province, and Qinghai Province (NBS, 2021). Numerous hazardous wastes are generated amid the metal ore processing and smelting processes (Wang et al., 2021), severely threatening the atmosphere, water environment, other ecological environments, and human health. The coal mining activities in Inner Mongolia Autonomous Region have caused a sharp decrease in lake area: 64.6% of the sharp decrease in lakes resulted from the water consumption for coal mining (Tao et al., 2015). The threat of PCL might extend to a radius of 70 km from the mining locale (Sonter et al., 2017), leading to water and soil degradation along the river basin. The treatment zone of PCL in the upper reaches may cause a series of environmental issues to the lower reaches. The impact on Brahmaputra (or the Yarlung Zangbo Jiang) rivers might stem from the mining areas at extremely high altitudes in the QTP zone (MEE, 2014).

5 Conclusions

The vector datasets about China's PCL at 1990, 2000, 2010, and 2020 have been developed using data fusion technology based on high-resolution remote sensing images, a land-use/cover change database, data from web crawler, and other multisource data. The spatial distribution and transfer pattern of China's PCL have been analyzed in national-, regional-, and county-level scales, the hotspot distribution of these areas has been recognized, and the influencing factors for the variation of their pattern have been further discussed.

The vector data products about China's PCL developed and acquired based on multisource data fusion technology have high quality and reliability, with an

overall accuracy of 93.21%. The overall area of China's PCL has kept growing since 1990, with significant differences across different time intervals. During 2000–2010, the growth rate of areas was 2.32 and 6.13 times that during 1990–2000 and 2010–2020, respectively. The agglomeration of China's PCL intensified and enlarged its sphere, and rendered the phenomenon of transferring from the N and SE zones to the NW, SW, and QTP zones during 1990–2020. The spatial pattern and transformation of China's PCL are joint effects of policies, mineral resources, economy, and other factors over the past 30 yr, among which policy and economy factors have contributed more prominently to the long time-sequence transition of areas.

The ecological-environmental problems in the PCL have attracted great attention in China. The results of this study provide scientific information about PCL and provide directions for local environmental protection departments and ecological governance. Subsequent research could begin with the comparison of transport models of different compounds and sites in different industries. The more detailed analyses of ecosystem services, such as comparing soil conservation and biodiversity protection functions with those of the pre-state to improve the ecological environment of the PCL in a more targeted way.

References

- Ahmed A I, Bryant R G, Edwards D P, 2021. Where are mines located in sub Saharan Africa and how have they expanded overtime? *Land Degradation & Development*, 32(1): 112–122. doi: [10.1002/ldr.3706](https://doi.org/10.1002/ldr.3706)
- Bernhardt E S, Lutz B D, King R S et al., 2012. How many mountains can we mine? assessing the regional degradation of Central Appalachian rivers by surface coal mining. *Environmental Science & Technology*, 46(15): 8115–8122. doi: [10.1021/es301144q](https://doi.org/10.1021/es301144q)
- Boldi P, Codenotti B, Santini M et al., 2004. Ubcrawler: a scalable fully distributed web crawler. *Software: Practice and Experience*, 34(8): 711–726. doi: [10.1002/spe.587](https://doi.org/10.1002/spe.587)
- Chakrabarti S, van den Berg M, Dom B, 1999. Focused crawling: a new approach to topic-specific Web resource discovery. *Computer Networks*, 31(11-16): 1623–1640. doi: [10.1016/S1389-1286\(99\)00052-3](https://doi.org/10.1016/S1389-1286(99)00052-3)
- Chen J, Chen J, Liao A P et al., 2015. Global land cover mapping at 30 m resolution: a POK-based operational approach. *ISPRS Journal of Photogrammetry and Remote Sensing*, 103: 7–27. doi: [10.1016/j.isprsjprs.2014.09.002](https://doi.org/10.1016/j.isprsjprs.2014.09.002)

- Cribari V, Strager M P, Maxwell A E et al., 2021. Landscape changes in the southern coalfields of west Virginia: multi-level intensity analysis and surface mining transitions in the headwaters of the coal river from 1976 to 2016. *Land*, 10(7): 748. doi: [10.3390/land10070748](https://doi.org/10.3390/land10070748)
- Deng M, Liu Q L, Cheng T et al., 2011. An adaptive spatial clustering algorithm based on delaunay triangulation. *Computers, Environment and Urban Systems*, 35(4): 320–332. doi: [10.1016/j.compenvurbsys.2011.02.003](https://doi.org/10.1016/j.compenvurbsys.2011.02.003)
- Endl A, Tost M, Hitch M et al., 2021. Europe's mining innovation trends and their contribution to the sustainable development goals: blind spots and strong points. *Resources Policy*, 74: 101440. doi: [10.1016/j.resourpol.2019.101440](https://doi.org/10.1016/j.resourpol.2019.101440)
- Gallwey J, Robiati C, Coggan J et al., 2020. A Sentinel-2 based multispectral convolutional neural network for detecting artisanal small-scale mining in Ghana: applying deep learning to shallow mining. *Remote Sensing of Environment*, 248: 111970. doi: [10.1016/j.rse.2020.111970](https://doi.org/10.1016/j.rse.2020.111970)
- Gong P, Liu H, Zhang M N et al., 2019. Stable classification with limited sample: transferring a 30-m resolution sample set collected in 2015 to mapping 10-m resolution global land cover in 2017. *Science Bulletin*, 64(6): 370–373. doi: [10.1016/j.scib.2019.03.002](https://doi.org/10.1016/j.scib.2019.03.002)
- Gong P, Li X C, Wang J et al., 2020. Annual maps of global artificial impervious area (GAIA) between 1985 and 2018. *Remote Sensing of Environment*, 236: 111510. doi: [10.1016/j.rse.2019.111510](https://doi.org/10.1016/j.rse.2019.111510)
- Guo Changqing, Chi Wenfeng, Kuang Wenhui et al., 2022. Mapping and spatio-temporal changes analysis of energy mining and producing sites in China using multi-source data from 1990 to 2020. *Journal of Geo-Information Science*, 24(1): 127–140. (in Chinese)
- He C Y, Liu Z F, Gou S Y, 2019. Detecting global urban expansion over the last three decades using a full convolutional network. *Environmental Research Letters*, 14(3): 034008. doi: [10.1088/1748-9326/aaf936](https://doi.org/10.1088/1748-9326/aaf936)
- Jiang Y F, Wang H L, Lei M, 2021. An integrated assessment methodology for management of potentially contaminated sites based on public data. *Science of the Total Environment*, 783: 146913. doi: [10.1016/j.scitotenv.2021.146913](https://doi.org/10.1016/j.scitotenv.2021.146913)
- Kausar A, Dhaka V S, Singh S K, 2013. Web crawler: a review. *International Journal of Computer Applications*, 63(2): 31–36. doi: [10.5120/10440-5125](https://doi.org/10.5120/10440-5125)
- Kim K, Park O, Barr J et al., 2019. Tourists' shifting perceptions of UNESCO heritage sites: lessons from Jeju Island-South Korea. *Tourism Review*, 74(1): 20–29. doi: [10.1108/TR-09-2017-0140](https://doi.org/10.1108/TR-09-2017-0140)
- Kimijima S, Sakakibara M, Nagai M et al., 2021. Time-series assessment of camp-type artisanal and small-scale gold mining sectors with large influxes of miners using Landsat imagery. *International Journal of Environmental Research and Public Health*, 18(18): 9441. doi: [10.3390/ijerph18189441](https://doi.org/10.3390/ijerph18189441)
- Kuang W H, Liu J Y, Dong J W et al., 2016. The rapid and massive urban and industrial land expansions in China between 1990 and 2010: a CLUD-based analysis of their trajectories, patterns, and drivers. *Landscape and Urban Planning*, 145: 21–33. doi: [10.1016/j.landurbplan.2015.10.001](https://doi.org/10.1016/j.landurbplan.2015.10.001)
- Kuang W H, Liu J Y, Tian H Q et al., 2022. Cropland redistribution to marginal lands undermines environmental sustainability. *National Science Review*, 9(1): nwab091. doi: [10.1093/nsr/nwab091](https://doi.org/10.1093/nsr/nwab091)
- Li H K, Xu F, Li Q, 2020. Remote sensing monitoring of land damage and restoration in rare earth mining areas in 6 counties in southern Jiangxi based on multisource sequential images. *Journal of Environmental Management*, 267: 110653. doi: [10.1016/j.jenvman.2020.110653](https://doi.org/10.1016/j.jenvman.2020.110653)
- Li T K, Liu Y, Bjerg P L, 2021. Prioritization of potentially contaminated sites: a comparison between the application of a solute transport model and a risk-screening method in China. *Journal of Environmental Management*, 281: 111765. doi: [10.1016/j.jenvman.2020.111765](https://doi.org/10.1016/j.jenvman.2020.111765)
- Li W W, Yang C W, Yang C J, 2010. An active crawler for discovering geospatial web services and their distribution pattern—a case study of OGC Web Map Service. *International Journal of Geographical Information Science*, 24(8): 1127–1147. doi: [10.1080/13658810903514172](https://doi.org/10.1080/13658810903514172)
- Liu X P, Hu G H, Chen Y M et al., 2018. High-resolution multi-temporal mapping of global urban land using Landsat images based on the Google Earth Engine platform. *Remote Sensing of Environment*, 209: 227–239. doi: [10.1016/j.rse.2018.02.055](https://doi.org/10.1016/j.rse.2018.02.055)
- Luckeneder S, Giljum S, Schaffartzik A et al., 2021. Surge in global metal mining threatens vulnerable ecosystems. *Global Environmental Change*, 69: 102303. doi: [10.1016/j.gloenvcha.2021.102303](https://doi.org/10.1016/j.gloenvcha.2021.102303)
- Maus V, Giljum S, Gutschlhofer J et al., 2020. A global-scale data set of mining areas. *Scientific Data*, 7(1): 289. doi: [10.1038/s41597-020-00624-w](https://doi.org/10.1038/s41597-020-00624-w)
- MEE (Ministry of Ecology and Environment of the People's Republic of China), 2014. Available at: http://www.gov.cn/xinwen/2014-04/17/content_2661765.htm. Cited 20 October 2021.
- NBS (National Bureau of Statistics of the People's Republic of China), 2021. Available at: <http://www.stats.gov.cn/>. Cited 20 October 2021.
- Ning J, Liu J Y, Kuang W H et al., 2018. Spatiotemporal patterns and characteristics of land-use change in China during 2010–2015. *Journal of Geographical Sciences*, 28(5): 547–562. doi: [10.1007/s11442-018-1490-0](https://doi.org/10.1007/s11442-018-1490-0)
- Nortcliff S, 2001. Sampling and pre-treatment—some observations from the United Kingdom. *Science of the Total Environment*, 264(1–2): 163–168. doi: [10.1016/S0048-9697\(00\)00619-7](https://doi.org/10.1016/S0048-9697(00)00619-7)
- Okabe A, Satoh T, Sugihara K, 2009. A kernel density estimation method for networks, its computational method and a GIS-based tool. *International Journal of Geographical Information Science*, 23(1): 7–32. doi: [10.1080/13658810802475491](https://doi.org/10.1080/13658810802475491)
- Owusu-Nimo F, Mantey J, Nyarko K B et al., 2018. Spatial distribution patterns of illegal artisanal small scale gold mining (*Galamsey*) operations in Ghana: a focus on the Western Region. *Heliyon*, 4(2): e00534. doi: [10.1016/j.heliyon.2018.02.005](https://doi.org/10.1016/j.heliyon.2018.02.005)

e00534

- Palmer M A, Bernhardt E S, Schlesinger W H et al., 2010. Mountaintop mining consequences. *Science*, 327(5962): 148–149. doi: [10.1126/science.1180543](https://doi.org/10.1126/science.1180543)
- Peng Y, Zhang Z M, He G J et al., 2019. An improved GrabCut method based on a visual attention model for rare-earth ore mining area recognition with high-resolution remote sensing images. *Remote Sensing*, 11(8): 987. doi: [10.3390/rs11080987](https://doi.org/10.3390/rs11080987)
- Pericak A A, Thomas C J, Kroodsma D A et al., 2018. Mapping the yearly extent of surface coal mining in Central Appalachia using Landsat and Google Earth Engine. *PLoS One*, 13(7): e0197758. doi: [10.1371/journal.pone.0197758](https://doi.org/10.1371/journal.pone.0197758)
- Rampanelli G B, Braun A B, Visentin C et al., 2021. The process of selecting a method for identifying potentially contaminated sites—a case study in a municipality in Southern Brazil. *Water, Air, & Soil Pollution*, 232(1): 26. doi: [10.1007/s11270-020-04970-8](https://doi.org/10.1007/s11270-020-04970-8)
- Rojano R E, Manzano C A, Toro R A et al., 2018. Potential local and regional impacts of particulate matter emitted from one of the world's largest open-pit coal mines. *Air Quality, Atmosphere & Health*, 11(5): 601–610. doi: [10.1007/s11869-017-0542-4](https://doi.org/10.1007/s11869-017-0542-4)
- Saley A A, Baratoux D, Baratoux L et al., 2021. Evolution of the koma bangou gold panning site (Niger) from 1984 to 2020 using Landsat imagery. *Earth and Space Science*, 8(11): e2021EA001879. doi: [10.1029/2021EA001879](https://doi.org/10.1029/2021EA001879)
- SCPRC (State Council of the People's Republic of China), 2013. Air pollution prevention and control action plan. Available at: http://www.gov.cn/zwgg/2013-09/12/content_2486773.htm. Cited 20 October 2021.
- SCPRC, 2015. Water pollution prevention and control action plan. Available at: http://www.gov.cn/zhengce/content/2015-04/16/content_9613.htm. Cited 20 October 2021.
- SCPRC, 2016. Soil pollution prevention and control action plan. Available at: http://www.gov.cn/zhengce/content/2016-05/31/content_5078377.htm. Cited 20 October 2021.
- Song Z C, Wang C, Ding L et al., 2021. Soil mercury pollution caused by typical anthropogenic sources in China: evidence from stable mercury isotope measurement and receptor model analysis. *Journal of Cleaner Production*, 288: 125687. doi: [10.1016/j.jclepro.2020.125687](https://doi.org/10.1016/j.jclepro.2020.125687)
- Sonter L J, Herrera D, Barrett D J et al., 2017. Mining drives extensive deforestation in the Brazilian Amazon. *Nature Communications*, 8(1): 1013. doi: [10.1038/s41467-017-00557-w](https://doi.org/10.1038/s41467-017-00557-w)
- Sonter L J, Dade M C, Watson J E M et al., 2020. Renewable energy production will exacerbate mining threats to biodiversity. *Nature Communications*, 11(1): 4174. doi: [10.1038/s41467-020-17928-5](https://doi.org/10.1038/s41467-020-17928-5)
- Tang L, Liu X M, Wang X Q et al., 2020. Statistical analysis of tailings ponds in China. *Journal of Geochemical Exploration*, 216: 106579. doi: [10.1016/j.gexplo.2020.106579](https://doi.org/10.1016/j.gexplo.2020.106579)
- Tang L, Werner T T, Xie H P et al., 2021. A global-scale spatial assessment and geodatabase of mine areas. *Global and Planetary Change*, 204: 103578. doi: [10.1016/j.gloplacha.2021.103578](https://doi.org/10.1016/j.gloplacha.2021.103578)
- Tao S L, Fang J Y, Zhao X et al., 2015. Rapid loss of lakes on the Mongolian Plateau. *Proceedings of the National Academy of Sciences of the United States of America*, 112(7): 2281–2286. doi: [10.1073/pnas.1411748112](https://doi.org/10.1073/pnas.1411748112)
- UN (United Nations), 2015. Transformation our world: the 2030 agenda for sustainable development A/RES/70/1. Available at: <http://undocs.org/en/A/RES/70/1>.
- Walker L R, 1999. Ecosystems of disturbed ground. In: *Ecosystems of the World*. Amsterdam: Elsevier, 16.
- Wang Fei, Zhang Manli, Wang Xuejiao et al., 2021. Generation and pollution characteristics of hazardous wastes from smelting of copper, lead and zinc in China. *Journal of Environmental Engineering Technology*, 11(5): 1012–1019. (in Chinese)
- Wang Z X, Chen J Q, Chai L Y et al., 2011. Environmental impact and site-specific human health risks of chromium in the vicinity of a ferro-alloy manufactory, China. *Journal of Hazardous Materials*, 190(1-3): 980–985. doi: [10.1016/j.jhazmat.2011.04.039](https://doi.org/10.1016/j.jhazmat.2011.04.039)
- Werner T T, Mudd G M, Schipper A M et al., 2020. Global-scale remote sensing of mine areas and analysis of factors explaining their extent. *Global Environmental Change*, 60: 102007. doi: [10.1016/j.gloenvcha.2019.102007](https://doi.org/10.1016/j.gloenvcha.2019.102007)
- Yang H, Huang X J, Thompson J R et al., 2014. China's soil pollution: urban brownfields. *Science*, 344(6185): 691–692. doi: [10.1126/science.344.6185.691-b](https://doi.org/10.1126/science.344.6185.691-b)
- Yuan D Z, Hu Z Q, Yang K et al., 2021. Assessment of the ecological impacts of coal mining and restoration in alpine areas: a case study of the Muli coalfield on the Qinghai-Tibet Plateau. *IEEE Access*, 9: 162919–162934. doi: [10.1109/ACCESS.2021.3133478](https://doi.org/10.1109/ACCESS.2021.3133478)
- Zeng X J, Liu Z F, He C Y et al., 2017. Detecting surface coal mining areas from remote sensing imagery: an approach based on object-oriented decision trees. *Journal of Applied Remote Sensing*, 11(1): 015025. doi: [10.1117/1.JRS.11.015025](https://doi.org/10.1117/1.JRS.11.015025)
- Zhang C, Kuang W H, Wu J G et al., 2021. Industrial land expansion in rural China threatens environmental securities. *Frontiers of Environmental Science & Engineering*, 15(2): 29. doi: [10.1007/s11783-020-1321-2](https://doi.org/10.1007/s11783-020-1321-2)
- Zhang X, Liu L Y, Wu C S et al., 2020. Development of a global 30 m impervious surface map using multisource and multitemporal remote sensing datasets with the Google Earth Engine platform. *Earth System Science Data*, 12(3): 1625–1648. doi: [10.5194/essd-12-1625-2020](https://doi.org/10.5194/essd-12-1625-2020)
- Zhang Z X, Wang X, Zhao X L et al., 2014. A 2010 update of National Land Use/Cover Database of China at 1: 100000 scale using medium spatial resolution satellite images. *Remote Sensing of Environment*, 149: 142–154. doi: [10.1016/j.rse.2014.04.004](https://doi.org/10.1016/j.rse.2014.04.004)